Multidecadal changes in ocean transparency: Decrease in a coastal upwelling region and increase offshore

Mati Kahru [1]*, **Zhongping Lee** [2], **Mark D. Ohman** [1]
[1]Scripps Institution of Oceanography, UCSD, La Jolla, California, USA
[2]College of Ocean and Earth Sciences, Xiamen University, Xiamen, China

Abstract

Detection of the effects of climate change on ocean ecosystems is often limited by the short duration of available time series. Here, we use ocean transparency measurements (the Secchi disk depth, Z_{SD}) in the California Current Ecosystem since 1949 and combine them with satellite estimates. Historic in situ measurements of Z_{SD} were irregular in space and time and are difficult to interpret in time series due to biases introduced by changing locations and timing. We normalize historic Z_{SD} measurements with satellite-derived mean climatology and create a merged in situ—satellite time series of Z_{SD} for the last ~ 73 yr. Although interannual variability in Z_{SD} is dominated by El Niño Southern Oscillation-related variability ($\sim 50\%$ of the total variance in many areas), a secular trend of decreasing transparency that is correlated with increasing productivity is detected 0–300 km from the coast in an area affected by coastal upwelling north of 27°N. In contrast, increasing transparency (correlated with decreasing productivity) is detected offshore (> 1000 km from the coast). In addition to those general trends, transparency is also increasing in coastal area off Baja California south of 27°N.

Oceanic phytoplankton play an important role in the global carbon budget and any changes in their productivity and composition are therefore of special interest for global climate change and biogeochemical cycling (Behrenfeld et al. 2016; Falkowski et al. 2008). A claim by Boyce et al. (2010, 2012, 2014) that global phytoplankton biomass has drastically declined over the last 100 yr has been challenged (McQuatters-Gollop et al. 2011 and others) and is affected by uncertainties in the available data. Climate-driven trends in global phytoplankton are typically evaluated using satellite data but these time series are relatively short and open to different interpretation (Behrenfeld et al. 2006, 2016; Martinez et al. 2009). Longer time series can be estimated using geochemical methods (Osman et al. 2019) or numerical models (Dutkiewicz et al. 2019; Cael et al. 2021).

Water transparency is an integrative variable that includes the effects of absorption by a wide variety of dissolved substances as well the effects of absorption and scattering by phytoplankton and non-algal particles (Preisendorfer 1986).

*Correspondence: mkahru@ucsd.edu

Water transparency affects processes such as primary production, solar bleaching of organic material, and phytoplankton physiology (Kirk 1994), as well as the encounter rates of zooplankton with fish (Aksnes and Giske 1993; Aksnes and Utne 1997) and zooplankton diel vertical migration behavior (Ohman and Romagnan 2016). Also, the other way round, processes like primary productivity and bleaching affect transparency. Water transparency can be measured with optical instruments and estimated with satellite sensors but a simple method called the Secchi disk depth (Z_{SD}, m) using the depth of disappearance of a white disk has been used for over a century (Tyler 1968; Preisendorfer 1986; Aksnes and Ohman 2009; Boyce et al. 2010; Pitarch 2020; Pitarch et al. 2021). Although the Secchi disk depth is a rather simple measurement, its advantage is the large number of measurements extending back many decades. Aksnes and Ohman (2009) documented a decrease in Z_{SD} in the nearshore region of the southern California Current Ecosystem (CCE) over the period 1969–2007. However, the variability was too large to detect any Z_{SD} trends offshore.

In oceanic waters, water transparency is closely correlated with phytoplankton concentration (typically measured as chlorophyll *a* [Chl *a*]; Falkowski and Wilson 1992) but is also sporadically reduced by river outflow plumes, other inputs of dissolved organic matter, and by resuspension of inorganic particles near the coast. Events such as phytoplankton blooms can markedly reduce Z_{SD}. All these events typically last from days to weeks. In contrast, on longer time scales, interannual

variability due to perturbations such as the El Niño Southern Oscillation (ENSO) and anomalous heatwaves (e.g., "the Blob," Bond et al. 2015) have strong effects on the whole marine ecosystem (Kahru and Mitchell 2000; Kahru et al. 2012, 2018; Jacox et al. 2018; Lilly et al. 2019) and can make it challenging to assess whether long-term secular changes have occurred in an ocean region. In the Baltic Sea, Dupont and Aksnes (2013) fitted an empirical relationship between Z_{SD} and the distance to coast and bottom depth to remove the mean effect of those two variables. However, such effects are not uniform in space and time. Kahru et al. (2022) removed both the mean spatial and seasonal variability in Z_{SD} using satellite-derived Z_{SD} climatology to further investigate centennial trends in the Baltic.

Here, we adopt the same approach as Kahru et al. (2022) and normalize historic shipborne Z_{SD} measurements by subtracting the mean 10-d seasonal Z_{SD} value of the nearest 4.5-km satellite pixel from each Z_{SD} measurement. We then compare in situ and satellite time series and merge them, in order to reconstruct a seven-decade record of water transparency in the CCE. The goal of this paper is to evaluate interannual variability and test for possible secular trends in water transparency in the CCE, using it as a proxy for primary productivity.

Data and methods

Satellite data

A number of models exist for calculating Z_{SD} from optical data (Preisendorfer 1986), but most are empirical in nature (Prasad et al. 1998) and less reliable in variable conditions. The algorithm of Lee et al. (2015), on the other hand, is based on new theoretical interpretation of sighting a Secchi disk in water, which adapts to the change in the spectral composition of sub-surface light. The algorithm and the model have been validated in different locations with different sensors (Lee et al. 2015, 2018; Liu et al. 2019; Kahru et al. 2022; Brewin et al. 2023).

The primary source of satellite data used here was the ESA Ocean Color Climate Change Initiative (OC-CCI) version 5.0 (Sathyendranath et al. 2019, https://esa-oceancolour-cci.org/). OC-CCI data were available from September 1997 to the end of 2021 and are merged from multiple ocean color sensors: SeaWiFS (1997–2010), MERIS (2002–2012), MODIS-Aqua (2002–2021), VIIRS-SNPP (2012–2021), and OLCI-A (2017–2021). We applied the Lee et al. (2015) Z_{SD} algorithm to OC-CCI daily remote sensing reflectance (R_{rs}) datasets of the six spectral bands (412, 443, 490, 510, 560, and 665 nm) at 4.5 km spatial resolution. We also used the diffuse attenuation coefficient at 490 nm (Kd_{490}, m^{-1}) derived following Lee et al. (2013), which is another common measure of water transparency (Preisendorfer 1986).

We calculated net primary production (NPP, mg C $m^{-2} d^{-1}$) using the well-known Vertically Generalized Productivity Model (VGPM) algorithm (Behrenfeld and Falkowski 1997) adapted to California Cooperative Oceanic Fisheries Investigations

Table 1. Number of in situ Secchi depth measurements per decade (*see* Fig. 1 for a map).

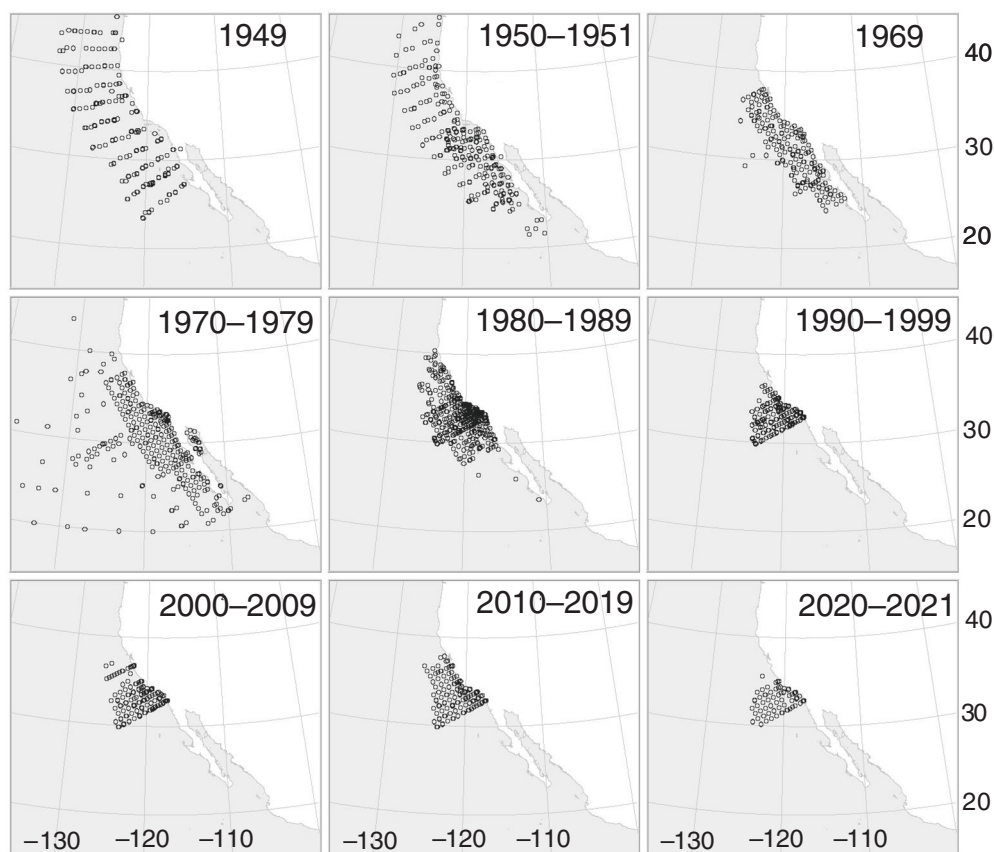| Decade	Number of in situ Secchi
−1949	320
1950–1959	475
1969	311
1970–1979	710
1980–1989	1075
1990–1999	1241
2000–2009	1138
2010–2019	1107
2020–2021	180
Total	6557

(CalCOFI) data (Kahru et al. 2009, 2020). As inputs, we used daily OC-CCI Chl *a* (mg m^{-3}), photosynthetically active radiation (PAR, merged from multiple sensors processed by NASA OBPG) and optimally interpolated daily sea-surface temperature (Reynolds et al. 2007). NPP was also estimated using the more recent CAFE model (Silsbe et al. 2016). Monthly CAFE model NPP products based on SeaWiFS and MODISA data were downloaded from http://sites.science.oregonstate.edu/ocean.productivity/index.php and merged.

Monthly anomalies of Z_{SD} and Kd_{490} were calculated for each pixel by removing the climatological monthly mean pixel value. Monthly Chl *a* and NPP anomalies were calculated by using the ratio of monthly mean value to the mean climatological value of the respective month. The ratio anomaly was then expressed as percentage anomaly with 100 * (Anomaly – 1).

In situ data

Aksnes and Ohman (2009) assembled in situ Z_{SD} data in the California Current region for 1949–2007. Most of these data were from the CalCOFI cruises conducted approximately quarterly (Ohman and Venrick 2003). We added additional measurements from the Southern California Bight Study (SCBS, 1975–1987, Eppley et al. 1985) and from recent CalCOFI cruises (https://calcofi.org/) until cruise 2021/11. Early Z_{SD} measurements (until 1969) were made with different methods (including with artificial lighting at night and a disk with black and white quadrants by day) and these were transformed and standardized by Aksnes and Ohman (2009). The total number of in situ Z_{SD} measurements assembled was 6557 for the time period 1949–2021 (Table 1). The locations of those in situ measurements changed over time (Fig. 1), with more extensive coverage in earlier decades. During the period of satellite data availability (beginning September 1998), the areal coverage of in situ data was more limited (Fig. 2A). We refer to that area as the main study area (MSA).

In situ Z_{SD} measurements were converted to Z_{SD} anomalies by subtracting the satellite-derived mean Z_{SD} value
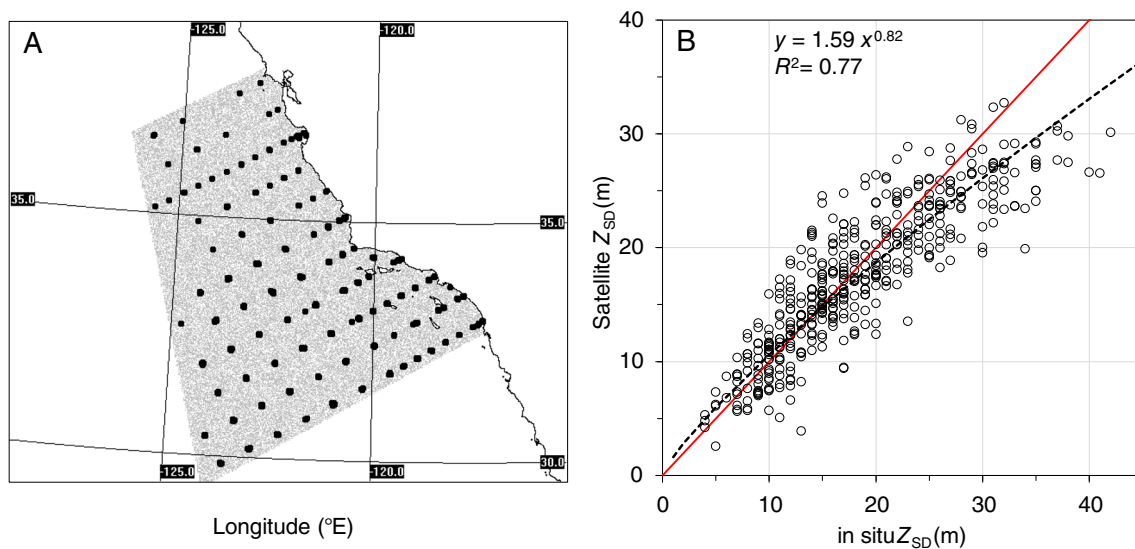
Fig. 1. Distribution of in situ Secchi depth (Z_{SD}) measurements in 1949–2021 along the west coast of North America.

(1997–2021) of the nearest pixel on a 4.5-km grid of the respective 10-d period of the annual cycle (*see* next section).

Normalization of Z_{SD} data

Satellite measurements over 25 yr (1997–2021) were used to create Z_{SD} and Kd_{490} mean climatologies (i.e., mean

Fig. 2. (**A**) MSA (gray) with in situ measurements (black dots) overlapping with satellite measurements (September 1998 to November 2021); (**B**) Match-ups of satellite-derived Z_{SD} against same day in situ measurements ($N = 443$, $r^2 = 0.77$). The circles show the mean satellite value in a 3×3 pixel area corresponding to the in situ measurement. Red line is the one-to-one line, black dashed line is the power function fit.

seasonal cycles) with 10-d temporal and 4.5 km spatial resolution. Examples of Z_{SD} and Kd_{490} climatologies averaged over coastal, transitional, and offshore domains for the area of Fig. 2A are shown in the Supporting Information (Fig. S1). Daily datasets were composited over 10-d periods by averaging valid pixel values (i.e., the composited value is the mean of 1–10 valid values). During cloudy periods this procedure still resulted in some missing pixel values. Those missing pixels in 10-d composites were filled by linear interpolation between corresponding valid values of previous and following 10-d composites. Corresponding 10-d periods over all available years were averaged to produce mean maps of satellite-derived Z_{SD} and Kd_{490} for each of the 10-d periods over a year (the last period consisted of either 5 or 6 d). These 37 datasets therefore consist of the mean pixel values for year days 1–10, 11–19, 20–29, and so on. The mean annual cycle for each pixel is made up of these 37 values.

Anomalies of in situ Z_{SD} were created by subtracting the respective climatology value of the nearest pixel in space and the 10-d period corresponding to the date of the measurement. This normalization of the numerous but spatially and temporally irregular historic samples made measurements in different areas (with different means) more comparable. The same procedure was applied to satellite data by subtracting the climatology value from the 10-d Z_{SD} and Kd_{490} composites. Z_{SD} anomalies were averaged over monthly periods to produce monthly anomalies that were subsequently averaged annually to produce annual Z_{SD} anomalies for both in situ and satellite values. Annual anomalies of each pixel were averaged over different spatial domains to produce time series for those domains.

As indices of ENSO, we used the Multivariate ENSO index (MEI.v2, Wolter and Timlin 2011; https://psl.noaa.gov/enso/mei/) and the San Diego detrended Sea Level Anomaly (SDSLA; Lilly and Ohman 2018). The SDSLA timeseries consists of monthly average sea-level anomalies, from which the seasonal cycle and long-term trend were removed, and, while correlated with equatorial indices of ENSO, is a more appropriate index of ENSO expression in this mid-latitude region (Lilly and Ohman 2018).

Potential trends in time series and their statistical significance were evaluated using the nonparametric Sen slope estimator (Sen 1968; Gilbert 1987) with the nonparametric Mann–Kendall test to evaluate the statistical significance of the trend (Salmi et al. 2002).

Results
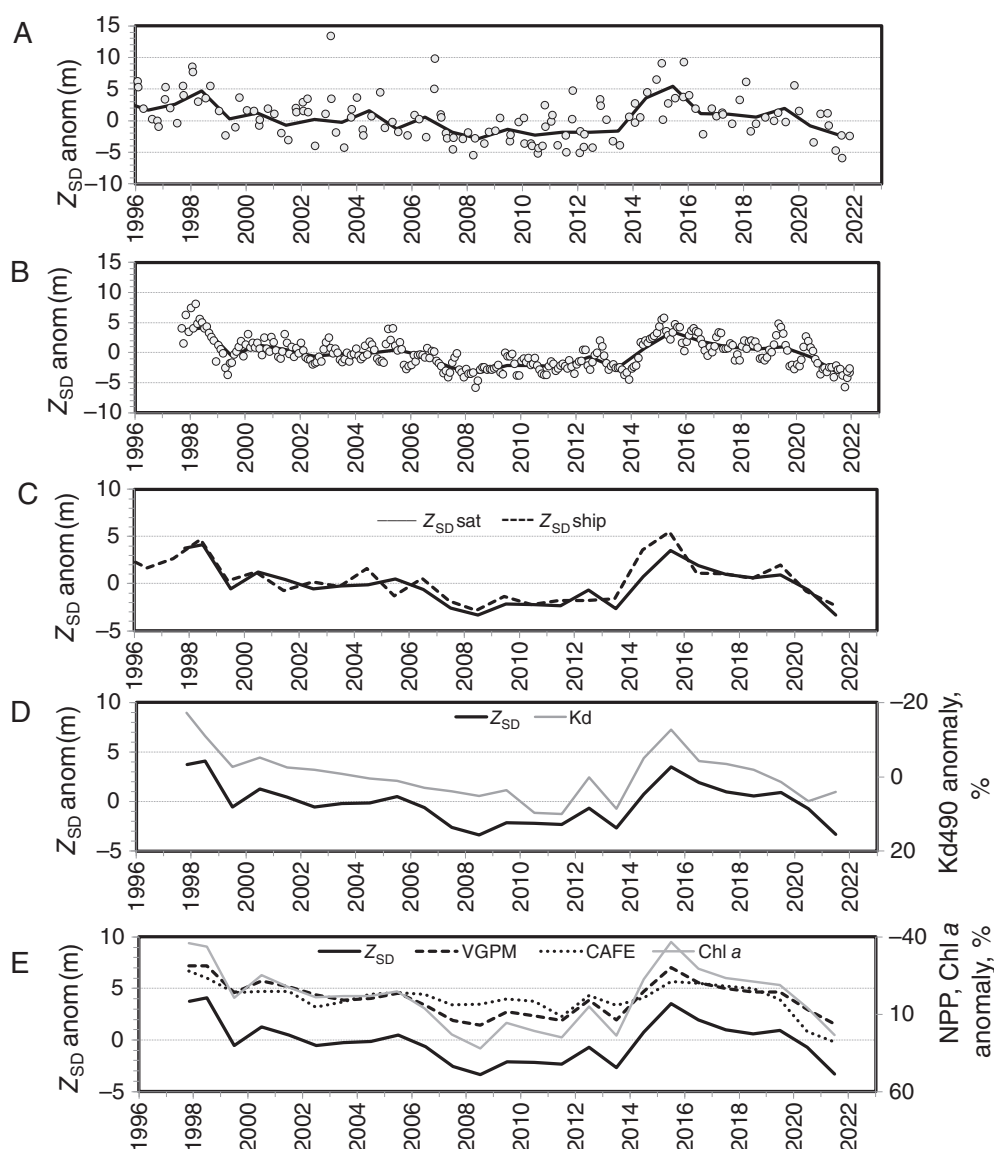
Validation of satellite estimates

The Lee et al. (2015) Z_{SD} model has been applied in a number of regions (Shang et al. 2016; Liu et al. 2020a,b; Kahru et al. 2022; Brewin et al. 2023). We validated the satellite-derived Z_{SD} datasets at daily and 4.5-km resolutions. We found a total of 443 same-day matchups with in situ measurements

and used the average pixel value in a 3×3 pixel window centered at the in situ measurement. Match-ups with high pixel-to-pixel variability ([Max − Min]/Min > 0.5) and with less than five valid pixels out of nine were excluded. The relationship between in situ and satellite Z_{SD} was evaluated using both the ordinary least squares linear regression and a Type II reduced major axis linear regression (York et al. 2004). We detected no significant bias between satellite and in situ data until Z_{SD} of about 30 m. At in situ $Z_{SD} > 30$ m, satellite-derived values underestimated the in situ values. To match satellite data product with in situ measurements for those deep Z_{SD} waters, we applied an empirical conversion by fitting a power function ($Y = 1.59 \times X^{0.82}$, where Y is satellite-derived Z_{SD} and X is in situ Z_{SD}) and then inverting it. We applied the conversion only for $Z_{SD} > 15$ m. The modified algorithm performed well ($r^2 = 0.77$, Fig. 2B) with a mean absolute percent difference $\sim 15\%$ and median absolute percent difference $\sim 11\%$. Some of the scatter around the curve is expected to be due to the difference in scale between an in situ point measurement and the mean of a 3×3 pixel area. The discrepancy at the clearest waters may be caused by problems with satellite estimates of R_{rs} as the Lee et al. (2015) algorithm has been shown to work well also in clear waters when using in situ R_{rs} data (Brewin et al. 2023). In conclusion, we assume that our converted satellite estimates of Z_{SD} are reasonably accurate and representative of in situ Secchi depth measurements.

Time series of Z_{SD} anomaly in the MSA

The MSA (Figs. 2A) was spatially well covered by both in situ and satellite measurements but the temporal coverage of the in situ data was restricted to approximately four cruises per year. The less frequent temporal coverage and the spatially less dense sampling probably explain why the monthly means of in situ Z_{SD} were more variable than the satellite-derived monthly means (Fig. 3A vs. Fig. 3B). However, the annual means of the in situ and satellite time series (Fig. 3C) were in good agreement ($r^2 = 0.78$, $p < 0.001$). The annual in situ Z_{SD} anomalies were slightly more variable than the satellite-derived annual averages. Interestingly, the biggest discrepancy between the satellite and in situ values was during the 2014–2015 warm anomaly when the in situ Z_{SD} values were higher than the satellite-derived values. Satellite-derived Kd_{490} (Fig. 3D) behaved like an inverse of the satellite-derived Z_{SD} with high correlation ($r^2 = 0.80$, $p < 0.001$). The minor differences may be due to the fact that Z_{SD} is based on the most transparent band that is not necessarily the 490-nm band. The most transparent spectral band in the CCE is typically the 443-nm band for offshore waters that switches to longer wavelengths in coastal waters. Annual anomalies in Z_{SD} are negatively correlated with anomalies of Chl a (Fig. 3E, $r^2 = 0.98$, $p < 0.001$) and NPP estimated with VGPM-CAL ($r^2 = 0.96$, $p < 0.001$) and CAFE ($r^2 = 0.75$, $p < 0.001$). It is notable that the coefficient of determination (r^2) is highest with Chl a, followed by VGPM-CAL, Kd_{490}, and CAFE.
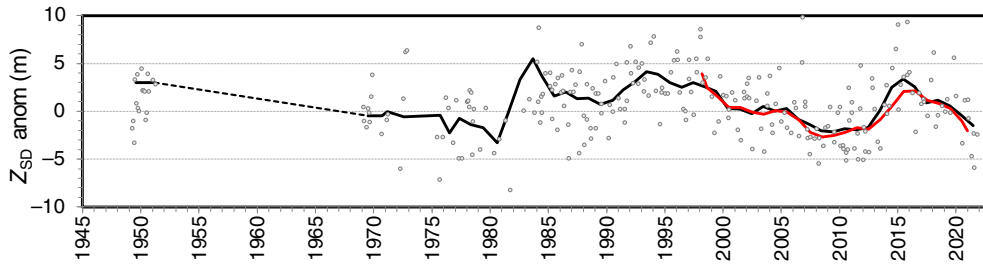
Fig. 3. Time series in the MSA (Fig. 2A). (**A**) Monthly (open circles) and annual (line) in situ Z_{SD} anomalies. (**B**) Monthly (open circles) and annual (line) satellite Z_{SD} anomalies. (**C**) Annual satellite (continuous line) and in situ (dashed) Z_{SD} anomalies. (**D**) Annual anomalies of satellite Z_{SD} (continuous black line, left axis) and Kd_{490} (gray continuous line, right axis, $\times 1000$). (**E**) Annual anomalies of satellite Z_{SD} (continuous black line, left axis), NPP according to VGPM-CAL (dashed black line, right axis) and the CAFE model (dotted black line, right axis) and satellite Chl a (continuous gray line, right axis). Note that the right axis is inverted.

As satellite-derived Z_{SD} estimates have better temporal and spatial coverage, we merge in situ and satellite data by using in situ values until 1997 and satellite-derived values from 1998 onward. The combined Z_{SD} anomaly time series averaged over the entire MSA for the 1949–2021 time period (Fig. 4) had a small linear decreasing trend of -0.03 m yr^{-1} that would result in decreasing Z_{SD} by 2.2 m over the 1949–2021 time period, but the trend was not statistically significant ($p = 0.13$) due to the large monthly and interannual variability. During the period of satellite data (1997–2021; Fig. 3B) the linear decreasing trend of monthly satellite-derived Z_{SD} anomaly in MSA was significant at $p < 0.05$ but not at $p < 0.01$. Monthly Z_{SD} means
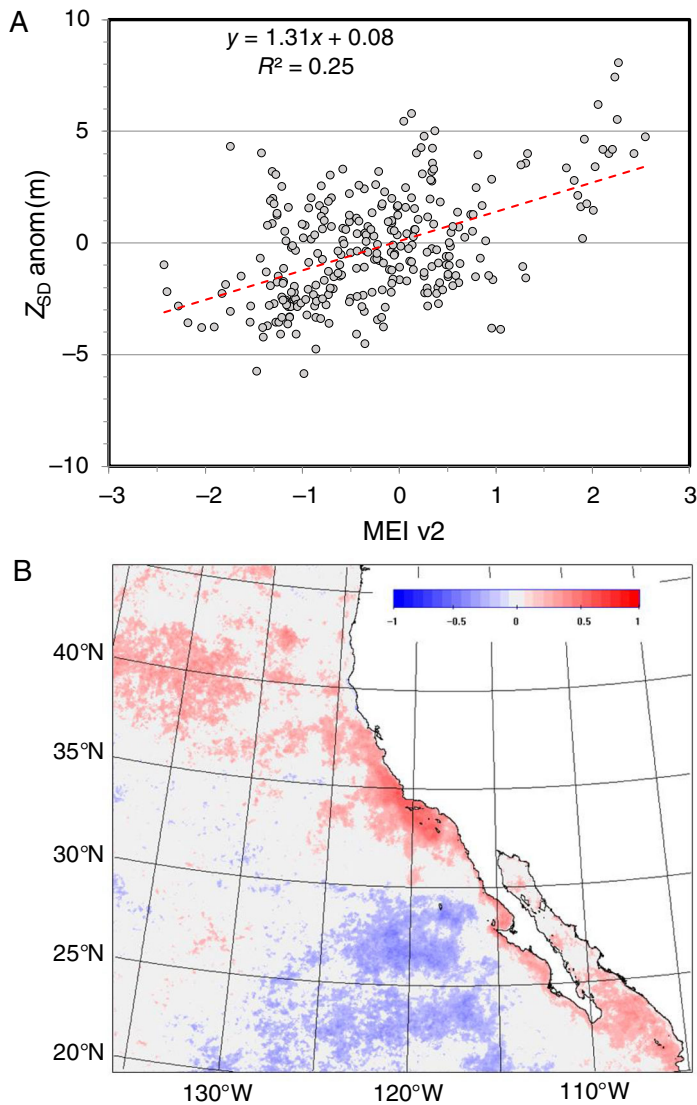
are correlated with ENSO indices such as MEI and SDSLA (Fig. 5). However, the strength and even the sign of the correlation is dependent on the location (Fig. 5B).

Time series of Z_{SD} anomaly in $1° \times 1°$ spatial bins

As temporal trends in Z_{SD} can be either positive or negative dependent on location, the trend estimates averaged over large areas, such as MSA, may be misleading. Although satellite time series can be evaluated at high spatial resolution, in situ data are spatially sparse. We therefore used $1° \times 1°$ spatial bins to evaluate trends in Z_{SD} time series. Due to the spatially and temporally irregular sampling pattern, particularly in the

Fig. 4. Time series of Z_{SD} anomalies in the main study area (Fig. 2A) showing in situ monthly averages (small gray circles), running 3-yr average of the annual in situ means (black line) and running 3-yr average of the annual satellite means (red line).
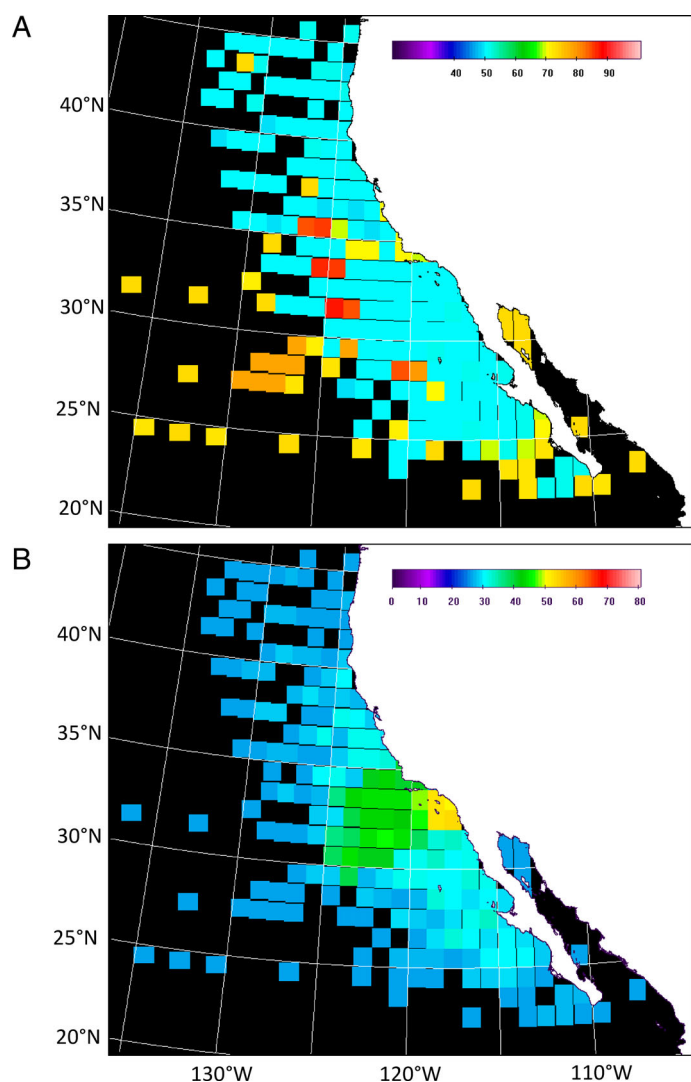

Fig. 5. (**A**) Relationship between the monthly Z_{SD} anomaly in MSA and the monthly multivariate ENSO index (MEI v2) along the west coast of North America; (**B**) Correlation coefficient (r) between satellite-derived monthly ZSD anomalies (1997–2021) and the San Diego detrended sea-level anomaly (SDSLA). r that is not significant at $p < 0.01$ is light gray.

early decades, the start year and the total number of years with Z_{SD} data were variable (Fig. 6). In most bins the measurements started around year 1950 (Fig. 6A) but were followed by a long gap (1952–1968; Table 1; Fig. 4). We considered bins with at least 26 yr of Z_{SD} data (i.e., 25 yr of satellite data and at least an additional 1 yr of in situ data). Most bins had at least 30 yr of data and the bins off southern California had 40–53 yr of data (Fig. 6b).
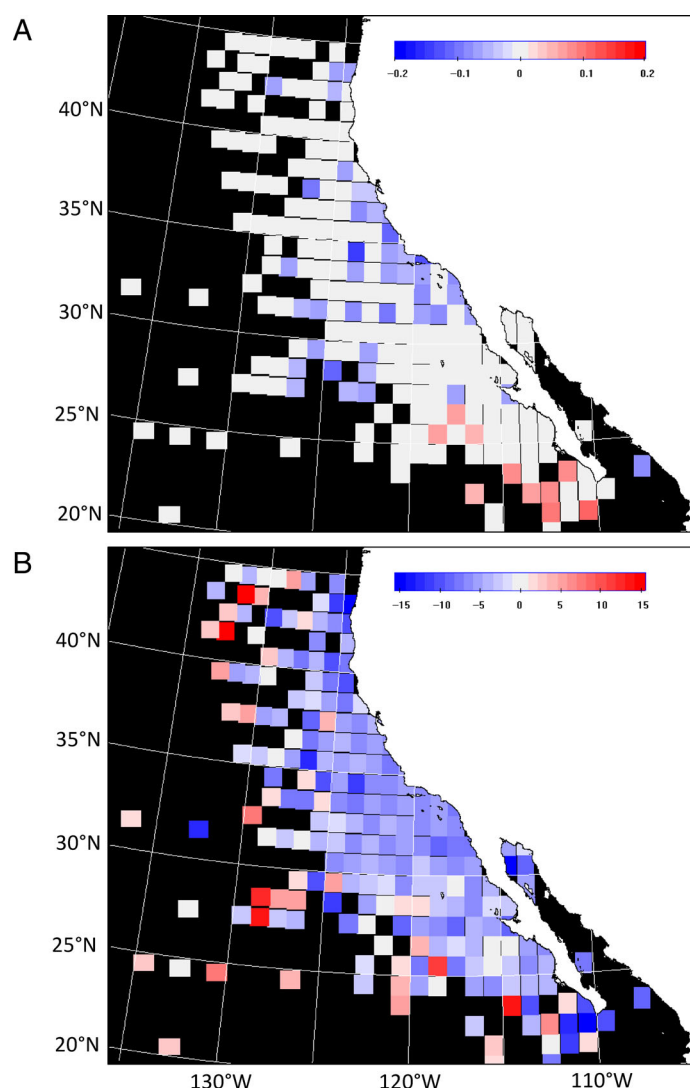
As Z_{SD} anomalies are correlated with the ENSO cycle in this region (Fig. 5), the time series can be biased by sampling during a particular phase of the ENSO cycle. This was particularly relevant during the early period when the number of sampled years was small and sampling was not annual. We therefore removed the average effect of ENSO in each $1° \times 1°$ spatial bin by subtracting the expected Z_{SD} value estimated from the ENSO index. We constructed linear regression models between an ENSO index (both MEI and SDSLA) and monthly Z_{SD} for each $1° \times 1°$ bin (like Fig. 5A) using satellite data of 1997–2021. We then removed the mean ENSO effect by subtracting the predicted monthly Z_{SD} value estimated from the monthly SDSLA index. The corrected monthly Z_{SD} values were then averaged annually.

After applying the nonparametric Sen slope estimator and masking all $1° \times 1°$ bins where the trend was not significant at 95% ($p < 0.05$), there were 40 bins with significant decreases and 10 bins with significant increases in Z_{SD} (Fig. 7A). The ENSO correction removed some of the scatter and improved the detection of change. The bins with decreasing Z_{SD} were primarily in coastal upwelling-affected areas along the coast of California and the bins with increasing Z_{SD} were in a limited region off southern Baja California. In the majority of bins, the trend estimated as the Sen slope was not significant. The Sen slope is estimated as the median of all possible slope estimates. Therefore, for bins with 25 yr of satellite data and only a few years of in situ data the Sen slope can be significant only if the trend is also present during the satellite period. In offshore areas with only a few years of presatellite measurements, the Sen slope would not detect a significant change even if there was a big jump between the early period (1949–1997) and the satellite-period. To evaluate the change from the presatellite period 1949–1997 to the present 1998–2021 period

Fig. 6. Combined in situ (1949–1997) and satellite (1997–2021) time series of the annual Z_{SD} anomalies in $1° \times 1°$ bins: (**A**) year of the first in situ measurement after 1900; (**B**) total number of years with available data.

Fig. 7. Combined in situ (1949–1997) and satellite (1997–2021) time series of the annual Z_{SD} anomalies in $1° \times 1°$ bins. (**A**) Sen slope of the change (m yr^{-1}) that is significant at $p < 0.05$. Slopes that are not significantly different from 0 are masked as white. (**B**) Change in the mean Z_{SD} anomaly (m) from 1949–1997 to 1998–2021.

we averaged the annual Z_{SD} anomalies during those two periods and calculated the change in the mean Z_{SD} (Fig. 7B). Although the dominance of decreasing Z_{SD} in coastal areas is similar to that detected by the Sen slope, its area is much wider. In contrast to the changes detected by the Sen slope, a number of offshore bins showed increasing Z_{SD}. That was not evident in the Sen slope pattern due to the relatively small number of annual values during the presatellite period. This shows that oceanic offshore waters have probably experienced a shift to increased Z_{SD} from ~ 1950 to present but the change is statistically difficult to prove due to the availability of only a few annual values from the presatellite period. The trend of increasing transparency in offshore waters becomes apparent when the change in Z_{SD} from the presatellite period to present (1998–2021) is pooled for three regions based on
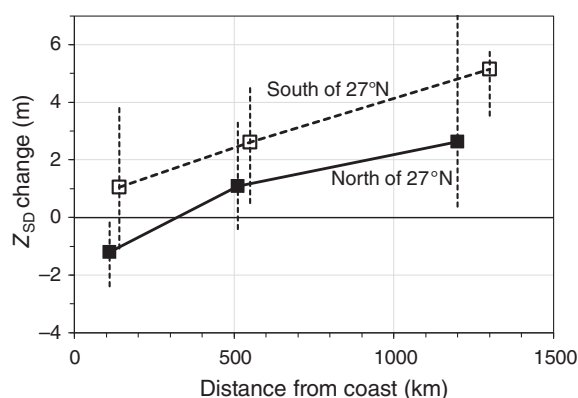
distance from the coast (Fig. 8). The 25–75% percentile range of Z_{SD} changes shows increasing Z_{SD} offshore, decreasing Z_{SD} in coastal (0–300 km) waters and intermediate trends in transition zone (300–1000 km).

Discussion

Water transparency is an important habitat characteristic for all aquatic organisms that are affected by light (Kirk 1994; Dupont and Aksnes 2013). In addition to in situ measurements, water transparency can be estimated with satellite ocean color data (Lee et al. 2015) with the advantage of consistent large-scale coverage at frequent intervals. High sampling frequency is essential to discover trends in areas of high variability. For example, around the Channel Islands in the

Fig. 8. Change in the mean Z_{SD} anomaly (m) from 1949–1997 to 1998–2021 in $1° \times 1°$ bins as a function of distance from coast: 0–300, 300–1000, and > 1000 km separated for south of 27°N (open squares, dashed line) and north of 27°N (filled squares, sold line). For each distance range the median (square) and the 25% to 75% percentile range (vertical dashed line) are given.

Southern California Bight where transparency is highly variable and affected by both plumes of sediment-rich turbid waters and blooms of phytoplankton (Otero and Siegel 2004), trends were difficult to detect in spite of over 50 yr of measurements.

In oceanic waters transparency is highly correlated with phytoplankton biomass (Chl *a*) and primary productivity (Fig. 3E). As transparency measurements are robust and much easier to make than in situ measurements of primary productivity, transparency can be used as a proxy to estimate trends in primary productivity. The high correlation among Chl *a*, Z_{SD}, NPP, and other satellite-derived variables is artificially increased when using satellite-derived estimates. All these products are derived from remote sensing reflectances that are inter-correlated and have few degrees of freedom (Cael et al. 2023). With these caveats in mind, it is not surprising that Z_{SD} may be better correlated with a model of primary production than different models of primary production using different input data with each other.

The trend of decreasing water transparency in the California Current coastal waters was first shown by Aksnes and Ohman (2009) who estimated a reduction in the Secchi depth by 0.06–0.13 m yr^{-1} in the nearshore region of the southern California Current over the period 1969–2007. Our merged time series confirm the general decrease in transparency in the upwelling-affected coastal areas but also show a spatially complex pattern with areas of increasing transparency and areas of decreasing transparency. Decreasing transparency (increasing productivity) is evident in most upwelling-affected areas along the coast of California excluding a limited area off Southern Baja California. Offshore oceanic waters, on the contrary, have increased transparency (decreased productivity) when comparing the pre-satellite ($\sim$ 1950–1997) period with the modern (1998–2021) period. Due to the small number of

measurements in the presatellite era, the statistical significance of that change can be problematic to prove.

Interannual variability associated with ENSO has a strong effect on water transparency and primary productivity and explains $\sim$ 50% of the total Z_{SD} variability in many locations. Although the long-term trends in water transparency and productivity are relatively small compared to their interannual variability, they are likely to have significant long-term effects on the ecosystem in the California Current area. This underscores the importance of sustaining long records in order for underlying trends to emerge from background variability (Hameau et al. 2019).

Our results support the conclusions drawn from multiple previous studies that the effect of global climate change and warming of the upper ocean is leading to decrease of productivity in ocean gyres (Polovina et al. 2008; Kahru et al. 2009, 2012; Boyce et al. 2010, 2014; Behrenfeld et al. 2016; Osman et al. 2019; Meng et al. 2021; Leonelli et al. 2022) but increase in productivity in coastal zones (Kahru et al. 2009, 2012).

Conclusions

Time series of historic shipboard measurements of water transparency combined with modern satellite data show a long-term trend of decreasing transparency (increasing productivity) in the upwelling ecosystem of the California Current during 1949–2021 but an increasing transparency (decreasing productivity) in offshore waters. Although the secular changes are relatively small compared to the ENSO-type interannual variability, their long-term effects are likely to be significant on the functioning of the ecosystem.

Data availability statement

The in situ Secchi depth dataset is at the Environmental Data Initiative (EDI) portal at https://pasta.lternet.edu/package/eml/knb-lter-cce/314/1, DOI: 10.6073/pasta/5865eb7e8924a146692b3a8011112fdb. Satellite data are available at https://esa-oceancolour-cci.org/ and https://oceancolor.gsfc.nasa.gov. Z_{SD} was calculated from satellite data with *wam_zsd* that is part of the Wimsoft package (https://www.wimsoft.com/).

References

Aksnes, D. L., and J. Giske. 1993. A theoretical model of aquatic visual feeding. Ecol. Model. **67**: 233–250. doi:10.1016/0304-3800(93)90007-f

Aksnes, D. L., and A. C. W. Utne. 1997. A revised model of visual range in fish. Sarsia **82**: 137–147.

Aksnes, D. L., and M. D. Ohman. 2009. Multi-decadal shoaling of the euphotic zone in the southern sector of the California Current System. Limnol. Oceanogr. **54**: 1272–1281. doi:10.4319/lo.2009.54.4.1272

Behrenfeld, M. J., and P. G. Falkowski. 1997. Photosynthetic rates derived from satellite-based chlorophyll

concentration. Limnol. Oceanogr. **42**: 1–20. doi:10.4319/lo.1997.42.1.0001

Behrenfeld, M. J., and others. 2006. Climate-driven trends in contemporary ocean productivity. Nature **444**: 752–755. doi:10.1038/nature05317

Behrenfeld, M. J., R. T. O'Malley, E. S. Boss, T. K. Westberry, J. R. Graff, K. Halsey, A. Milligan, D. A. Siegel, and M. Brown. 2016. Revaluating ocean warming impacts on global phytoplankton. Nat. Clim. Change **6**: 323–330. doi:10.1038/nclimate2838

Bond, N. A., M. F. Cronin, H. Freeland, and N. Mantua. 2015. Causes and impacts of the 2014 warm anomaly in the NE Pacific. Geophys. Res. Lett. **42**: 3414–3420. doi:10.1002/2015GL063306

Boyce, D. G., M. R. Lewis, and B. Worm. 2010. Global phytoplankton decline over the past century. Nature **466**: 591–596. doi:10.1038/nature09268

Boyce, D., M. Lewis, and B. Worm. 2012. Integrating global chlorophyll data from 1890 to 2010. Limnol. Oceanogr. Methods **10**: 840–852. doi:10.4319/lom.2012.10.840/full

Boyce, D. G., M. Dowd, M. R. Lewis, and B. Worm. 2014. Estimating global chlorophyll changes over the past century. Prog. Oceanogr. **122**: 163–173. doi:10.1016/j.pocean.2014.01.004

Brewin, R. J. W., J. Pitarch, G. Dall'Olmo, H. J. van der Woerd, J. Lin, X. Sun, and G. H. Tilstone. 2023. Evaluating historic and modern optical techniques for monitoring phytoplankton biomass in the Atlantic Ocean. Front. Mar. Sci. **10**: 1111416. doi:10.3389/fmars.2023.1111416

Cael, B. B., S. Dutkiewicz, and S. Henson. 2021. Abrupt shifts in 21st-century plankton communities. Sci. Adv **7**: eabf8593. doi:10.1126/sciadv.abf8593

Cael, B. B., K. Bisson, E. Boss, and Z. Erickson. 2023. How many independent quantities can be extracted from ocean color? Limnol. Oceanogr. Lett. doi:10.1002/lol2.10319

Dupont, N., and D. L. Aksnes. 2013. Centennial changes in water clarity of the California Current and the North Sea. Estuar. Coast. Shelf Sci. **131**: 282–289. doi:10.1016/j.ecss.2013.08.010

Dutkiewicz, S., A. E. Hickman, O. Jahn, S. Henson, C. Beaulieu, and E. Monier. 2019. Ocean colour signature of climate change. Nat. Commun. **10**: 578.

Eppley, R., E. Steward, M. Abbott, and U. Heyman. 1985. Estimating ocean primary production from satellite chlorophyll: Introduction to regional differences and statistics for the Southern California Bight. J. Plankton Res. **7**: 57–70. doi:10.1093/plankt/7.1.57

Falkowski, P. G., and C. Wilson. 1992. Phytoplankton productivity in the North Pacific Ocean since 1900 and implications for absorption of anthropogenic CO_2. Nature **358**: 741–743. doi:10.1038/358741a0

Falkowski, P. G., T. Fenchel, and E. F. Delong. 2008. The microbial engines that drive Earth's biogeochemical cycles. Science **320**: 1034–1039. doi:10.1126/science.1153213

Gilbert, R. O. 1987. Statistical methods for environmental pollution monitoring. Van Nostrand Reinhold.

Hameau, A., J. Mignot, and F. Joos. 2019. Assessment of time of emergence of anthropogenic deoxygenation and warming: Insights from a CESM simulation from 850 to 2100 CE. Biogeosciences **16**: 1755–1780. doi:10.5194/bg-16-1755-2019

Jacox, M. G., M. A. Alexander, N. J. Mantua, J. D. Scott, G. Hervieux, R. S. Webb, and F. E. Werner. 2018. Forcing of multiyear extreme ocean temperatures that impacted California current living marine resources in 2016. Bull. Am. Meteorol. Soc. **99**: S27–S33.

Kahru, M., and B. G. Mitchell. 2000. Influence of the 1997–98 El Niño on the surface chlorophyll in the California Current. Geophys. Res. Lett. **27**: 2937–2940. doi:10.1029/2000GL011486

Kahru, M., R. Kudela, M. Manzano-Sarabia, and B. G. Mitchell. 2009. Trends in primary production in the California Current detected with satellite data. J. Geophys. Res. Ocean. **114**: 1–7. doi:10.1029/2008JC004979

Kahru, M., R. M. Kudela, M. Manzano-Sarabia, and B. G. Mitchell. 2012. Trends in the surface chlorophyll of the California Current: Merging data from multiple ocean color satellites. Deep. Res. Part II Top. Stud. Oceanogr. **77–80**: 89–98. doi:10.1016/j.dsr2.2012.04.007

Kahru, M., M. G. Jacox, and M. D. Ohman. 2018. CCE1: Decrease in the frequency of oceanic fronts and surface chlorophyll concentration in the California Current System during the 2014–2016 Northeast Pacific warm anomalies. Deep-Sea Res. **I**: 4–13. doi:10.1016/j.dsr.2018.04.007

Kahru, M., R. Goericke, T. B. Kelly, and M. R. Stukel. 2020. Satellite estimation of carbon export by sinking particles in the California Current calibrated with sediment trap data. Deep-Sea Research Part II **173**: 104639. doi:10.1016/j.dsr2.2019.104639

Kahru, M., H. Bittig, R. Elmgren, V. Fleming, Z. Lee, and G. Rehder. 2022. Baltic Sea transparency from ships and satellites: Centennial trends. Mar. Ecol. Prog. Ser. **697**: 1–13. doi:10.3354/meps14151

Kirk, J. T. O. 1994. Light and photosynthesis in aquatic ecosystems. Cambridge Univ. Press.

Lee, Z., S. Shang, C. Hu, K. Du, A. Weidemann, W. Hou, J. Lin, and G. Lin. 2015. Secchi disk depth: A new theory and mechanistic model for underwater visibility. Rem. Sens. Environ. **169**: 139–149. doi:10.1016/j.rse.2015.08.002

Lee, Z., S. Shang, K. Du, and J. Wei. 2018. Resolving the long-standing puzzles about the observed Secchi depth relationships. Limnol. Oceanogr. **63**. doi:10.1002/lno.10940

Lee, Z. P., C. Hu, S. Shang, K. Du, M. Lewis, R, Arnone, and R. Brewin. 2013. Penetration of UV – visible solar light in the global oceans: Insights from ocean color remote sensing. J. Geophys. Res. Ocean **118**: 4241–4255. doi:10.1002/jgrc.20308

Leonelli, F. E., M. Bellacicco, J. Pitarch, E. Organelli, B. Buongiorno Nardelli, V. de Toma, C. Cammarota, S. Marullo, and R. Santoleri. 2022. Ultra-oligotrophic waters expansion in the North Atlantic Subtropical Gyre revealed by 21 years of satellite observations. Geophys. Res. Lett. **49**: e2021GL096965. doi:10.1029/2021GL096965

Lilly, L. E., and M. D. Ohman. 2018. CCE IV: El Niño-related zooplankton variability in the southern California Current System. Deep-Sea Res. I Oceanogr. Res. Pap. **140**: 36–51. doi:10.1016/j.dsr.2018.07.015

Lilly, L. E., U. Send, M. Lankhorst, T. R. Martz, and M. D. Ohman. 2019. Biogeochemical anomalies at two southern California Current System moorings during the 2014-16 Warm Anomaly-El Niño sequence. J. Geophys. Res. Oceans **124**: 6886–6903. doi:10.1029/2019JC015255

Liu, X., Z.-P. Lee, Y. Zhang, J. Lin, K. Shi, Y. Zhou, B. Qin, and Z. Sun. 2019. Secchi depth remote sensing in highly turbid lake waters and its application with MERIS data. Remote Sens. **11**: 2226. doi:10.3390/rs11192226

Liu, X., X. Meng, X. Wang, D. Bi, L. Chen, and Q. Lou. 2020*a*. Using a semi-analytical model to retrieve Secchi depth in coastal and estuarine waters. Acta Oceanol. Sin. **39**: 103–112. doi:10.1007/s13131-020-1620-2

Liu, Y., X. Chenchao, J. Li, F. Zhang, and S. Wang. 2020*b*. Secchi disk depth estimation from China's new generation of GF-5 hyperspectral observations using a semi-analytical scheme. Remote Sens. (Basel) **12**: 1849. doi:10.3390/rs12111849

Martinez, E., D. Antoine, F. D'Ortenzio, and B. Gentili. 2009. Climate-driven basin-scale decadal oscillations of oceanic phytoplankton. Science **326**: 1253–1256. doi:10.1126/science.1177012

McQuatters-Gollop, A., and others. 2011. Is there a decline in marine phytoplankton? Nature **472**: E6–E7. doi:10.1038/nature09950

Meng, S., and others. 2021. Strengthening ocean desert process in the North Pacific over the past two decades. Environ. Res. Lett. **16**: 024034. doi:10.1088/1748-9326/abd96f

Ohman, M. D., and E. L. Venrick. 2003. CalCOFI in a changing ocean. Oceanography **16**: 76–85. doi:10.5670/oceanog.2003.34

Ohman, M. D., and J. B. Romagnan. 2016. Nonlinear effects of body size and optical attenuation on Diel Vertical Migration by zooplankton. Limnol. Oceanogr. **61**: 765–770. doi:10.1002/lno.10251

Osman, M. B., and others. 2019. Industrial-era decline in subarctic Atlantic productivity. Nature **569**: 551–555. doi:10.1038/s41586-019-1181-8

Otero, M. P., and D. A. Siegel. 2004. Spatial and temporal characteristics of sediment plumes and phytoplankton blooms in the Santa Barbara Channel. Deep Sea Res. II Topic. Stud. Oceanogr. **51**: 1129–1149. doi:10.1016/S0967-0645(04)00104-3

Pitarch, J. 2020. A review of Secchi's contribution to marine optics and the foundation of Secchi disk science. Oceanography **33**: 26–37. doi:10.5670/oceanog.2020.301

Pitarch, J., M. Bellacicco, S. Marullo, and H. van der Word. 2021. Global maps of Forel-Ule index, hue angle and Secchi disk depth derived from 21 years of monthly ESA Ocean Colour Climate Change Initiative data. Earth Syst. Sci. Data **13**: 481–490. doi:10.5194/essd-13-481-2021

Polovina, J. J., E. A. Howell, and M. Abecassis. 2008. Ocean's least productive waters are expanding. Geophys. Res. Lett. **35**: L36183. doi:10.1029/2007GL031745

Prasad, K. S., R. L. Bernstein, M. Kahru, and B. G. Mitchell. 1998. Ocean color algorithms for estimating water clarity (Secchi depth) from SeaWiFS. J. Adv. Mar. Sci. Tech. Soc. **4**: 301–306.

Preisendorfer, R. W. 1986. Secchi disk science: Visual optics of natural waters. Limnol. Oceanogr. **31**: 909–926. doi:10.4319/lo.1986.31.5.0909

Reynolds, R. W., T. M. Smith, C. Liu, D. B. Chelton, K. S. Casey, and G. Schlax. 2007. Daily high-resolution blended analyses for sea surface temperature. J. Climate **20**: 5473–5496. doi:10.1175/2007JCLI1824.1

Salmi, T., A. Määttä, P. Anttila, T. Ruoho-Airola, and T. Amnell. 2002. Detecting trends of annual values of atmospheric pollutants by the Mann–Kendall test and Sen's slope estimates—The excel template application MAKESENS. Finnish Meteorological Institute. Publications on air quality, v. **31**, Report Code FMI-AQ-31. p. 35.

Sathyendranath, S., R. Brewin, C. Brockmann, V. Brotas, B. Calton, A. Chuprin, and T. Platt. 2019. An ocean-colour time series for use in climate studies: The experience of the ocean-colour climate change initiative (OC-CCI). Sensors **19**: 4285. doi:10.3390/s19194285

Sen, P. K. 1968. Estimates of the regression coefficient based on Kendall's tau. J. Am. Stat. Assoc. **63**: 1379–1389.

Shang, S., Z. Lee, L. Shi, G. Lin, G. Wei, and X. Li. 2016. Changes in water clarity of the Bohai Sea: Observations from MODIS. Remote Sens. Environ. **186**: 22–31. doi:10.1016/j.rse.2016.08.020

Silsbe, G. M., M. J. Behrenfeld, K. H. Halsey, A. J. Milligan, and T. K. Westberry. 2016. The cafe model: A net production model for global ocean phytoplankton. Global Biogeochem. Cycl. **30**: 1756–1777. doi:10.1002/2016GB005521

Tyler, J. E. 1968. The Secchi disc. Limnol. Oceanogr. **13**: 1–6. doi:10.4319/lo.1968.13.1.0001

Wolter, K., and M. S. Timlin. 2011. El Niño/Southern Oscillation behaviour since 1871 as diagnosed in an extended multivariate ENSO index (MEI.ext). Intl. J. Climatol. **31**: 1074–1087. doi:10.1002/joc.2336

York, D., N. M. Evensen, M. L. Martinez, and J. D. Delgado. 2004. Unified equations for the slope, intercept, and standard errors of the best straight line. Am. J. Phys. **72**: 367–375. doi:10.1119/1.1632486

Conflict of Interest

The authors declare no conflict of interest.
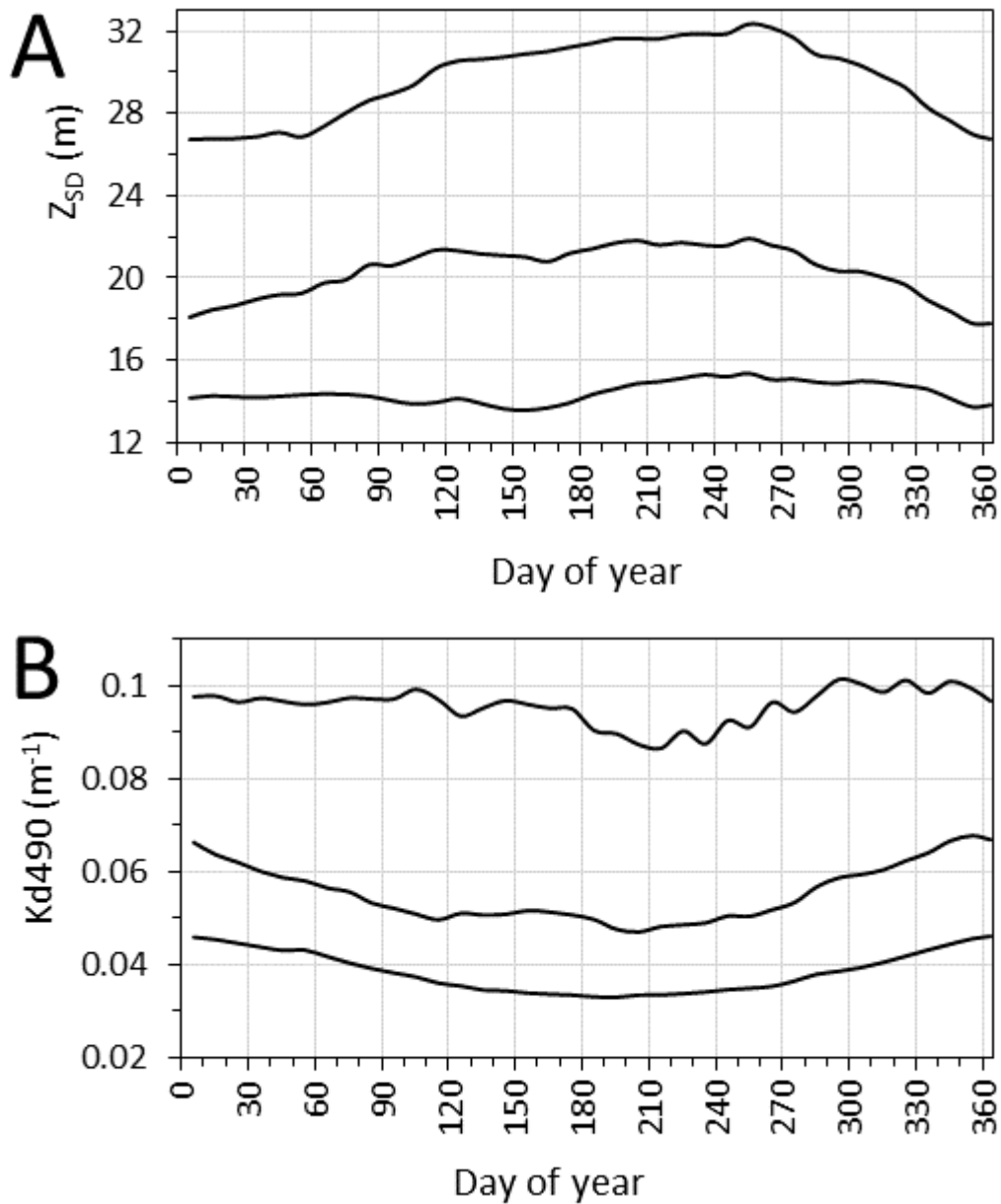
1   Multidecadal changes in ocean transparency: decrease in a coastal upwelling region and increase

2   offshore

3   Mati Kahru[1,*], Zhongping Lee[2], Mark D. Ohman[1]

4

5   *Supplement*

7   **Fig. S1.** Annual climatology of Z_{SD} (A) and Kd490 (B) in the area shown in Fig. 2A. The curves

8   are for mean values for three bands from coast: 0-300 km, 300-1000 km and >1000 km.